Main Manuscript for

A redox switch allows binding of ferrous and ferric ions in the cyanobacterial iron binding protein FutA from *Prochlorococcus*

Rachel Bolton[a,b], Moritz M. Machelett[a,c], Jack Stubbs[a,b], Danny Axford[b], Nicolas Caramello[d,e], Lucrezia Catapano[f,g], Martin Malý[a], Matthew J. Rodrigues[a,b,h], Charlotte Cordery[a,b], Graham J. Tizzard[i], Fraser MacMillan[j], Sylvain Engilberge[d], David von Stetten[k], Takehiko Tosha[l], Hiroshi Sugimoto[l], Jonathan A.R. Worrall[m], Jeremy S. Webb[a,b], Mike Zubkov[c,n], Simon Coles[i], Eric Mathieu[o], Roberto A. Steiner[f,p], Garib Murshudov[g], Tobias E. Schrader[q], Allen M. Orville[b,r], Antoine Royant[d,o], Gwyndaf Evans[b,s], Michael A. Hough[b,m,r], Robin L. Owen[b], Ivo Tews[a]

[a] Biological Sciences, Institute for Life Sciences, University of Southampton, Southampton, SO17 1BJ, UK

[b] Diamond Light Source, Harwell Science and Innovation Campus, Didcot, Oxfordshire, OX11 0DE, UK

[c] National Oceanography Centre, Southampton SO14 3ZH, UK

[d] European Synchrotron Radiation Facility, 38043 Grenoble Cedex 9, France

[e] Hamburg Centre for Ultrafast Imaging, HARBOR, Universität Hamburg, Luruper Chaussee 149, 22761 Hamburg, Germany

[f] Randall Centre of Cell and Molecular Biophysics, King's College London, New Hunt's House, Guy's Campus, London, SE1 1UL, UK

[g] MRC Laboratory of Molecular Biology, Francis Crick Avenue, Cambridge Biomedical Campus, Cambridge, CB2 0QH, UK

[h] Laboratory of Biomolecular Research, Paul Scherrer Institute, 5232 Villigen, Switzerland

[i] School of Chemistry, University of Southampton, Southampton, SO17 1BJ, UK

[j] School of Chemistry, University of East Anglia, Norwich NR4 7TJ, UK

[k] European Molecular Biology Laboratory (EMBL), Hamburg Unit, Notkestraße 85, 22607 Hamburg, Germany

[l] Synchrotron Radiation Life Science Instrumentation Team, RIKEN SPring-8 Center, 1-1-1 Kouto, Sayo, Hyogo 679-5148, Japan

[m] School of Life Sciences, University of Essex, Wivenhoe Park, Colchester CO4 3SQ, UK

[n] Scottish Association for Marine Science, Oban PA37 1QA, Scotland, UK

[o] Univ. Grenoble Alpes, CNRS, CEA, Institut de Biologie Structurale (IBS), 38044 Grenoble Cedex 9, France

[p] Department of Biomedical Sciences, University of Padova, Viale G. Colombo 3, 35131 Padova, Italy

[q] Forschungszentrum Jülich GmbH, Jülich Centre for Neutron Science (JCNS), Lichtenbergstraße 1, 85748 Garching, Germany

[r] Research Complex at Harwell, Harwell Science and Innovation Campus, Didcot, OX11 0FA, United Kingdom

[s] Rosalind Franklin Institute, Harwell Science and Innovation Campus, Didcot, Oxfordshire, OX11 0FA, UK

*Corresponding author: Ivo Tews, Biological Sciences, Institute for Life Sciences, University of Southampton, Southampton, SO17 1BJ, UK, m: ivo.tews@soton.ac.uk

Email: ivo.tews@soton.ac.uk

Author Contributions: Investigation: RB, MMM, JS, DA, NC, CC, GJT, FMM, SE, EM, TS, AR, MH, RLO, IT; Formal Analysis: RB, JS, DA, NC, LC, MM, MJR, FMM, TS, AR, IT; Methodology: DA, NC, LC, MJR, SE, DvS, TT, HS, JW, RAS, GM, TS, AR, MH, RLO, IT; Funding acquisition: JSW, MZ, SC, AMO, GE, MH, IT; Writing – original draft: RB, MoM, IT, Writing – review & editing: RB, DA, AMO, AR, MH, RLO, IT.

Competing Interest Statement: The authors do not declare competing interests.

Classification: Biological Sciences / Biophysics and Computational Biology.

Keywords: cyanobacteria, serial femtosecond crystallography, radiation damage, iron, ABC transporter.

This PDF file includes:

Main Text
Figures 1 to 4

Abstract

The marine cyanobacterium *Prochlorococcus* is a main contributor to global photosynthesis, whilst being limited by iron availability. Cyanobacterial genomes typically encode two different types of FutA iron binding proteins: periplasmic FutA2 ABC transporter subunits bind ferric (Fe^{3+}), while cytosolic FutA1 binds ferrous (Fe^{2+}). Owing to their small size and their economized genome *Prochlorococcus* ecotypes typically possess a single *futA* gene. How the encoded FutA protein might bind different Fe oxidation states was previously unknown. Here we use structural biology techniques at room temperature to probe the dynamic behavior of FutA. Neutron diffraction confirmed four negatively charged tyrosinates, that together with a solvent molecule coordinate iron in trigonal bipyramidal geometry. Positioning of the positively charged Arg103 side chain in the second coordination shell was consistent with an overall charge-neutral ferric binding state in structures determined by neutron diffraction and serial femtosecond crystallography. Conventional rotation X-ray crystallography using a home source revealed X-ray induced photoreduction of the iron center with observation of the ferrous binding state; here, an additional positioning of the Arg203 side chain in the second coordination shell maintained an overall charge neutral ferrous binding site. Room temperature dose series using serial synchrotron crystallography and an XFEL X-ray pump-probe approach capture the transition between ferric and ferrous states, revealing how Arg203 operates as a switch to accommodate the different iron oxidation states. This switching ability of the *Prochlorococcus* FutA protein may reflect ecological adaptation by genome streamlining and loss of specialized FutA proteins.

Significance Statement

Oceanic primary production by marine cyanobacteria is a main contributor to carbon and nitrogen fixation. *Prochlorococcus* is the most abundant photosynthetic organism on Earth, with an annual carbon fixation comparable to the net global primary production from agriculture. Its remarkable ecological success is based on the ability to thrive in low nutrient waters. To manage iron limitation, *Prochlorococcus* possesses the FutA protein for iron uptake and homeostasis. We reveal a switch in the FutA protein that allows it to accommodate binding of iron in either the ferric (Fe^{3+}) or ferrous (Fe^{2+}) state using structural biology techniques at room temperature and provide a plausible mechanism for FutA as a bifunctional redox state sensing protein.

Main Text

Introduction

Iron is the fourth most abundant element in the Earth's crust (1). However, because of its poor solubility, primary production in large oceanic and freshwater environments is limited by iron uptake (2). In oxygenated aqueous environments, iron predominantly exists in the ferric (Fe^{3+}) state with a solubility of 10^{-18} M (3). Ferric iron precipitates to form ferric oxyhydroxides (4) thought not to be generally bioavailable (5). Marine phytoplankton require iron in the photosynthetic electron transport chain (6) and in the nitrogenase enzyme (7, 8); thus, iron availability directly limits photosynthesis (9) and nitrogen fixation (10).

Cyanobacteria of the *Prochlorococcus* genus are able to fix four gigatons of carbon per annum, which is comparable to the net primary production of global agriculture (11). *Prochlorococcus* bacteria dominate bacterial populations in tropical and subtropical oligotrophic ocean regions (12). One of the factors for ecological success is the exceptional ability of this bacterium to thrive in low nutrient waters (13). Adaptation includes reduction in size to 0.5 – 0.7 μm, making *Prochlorococcus* not only the most abundant but also the smallest photosynthetic organism on Earth (14). Reduction in size maximizes the area-to-volume ratio for metabolic efficiency, to a tradeoff of genome reduction, and *Prochlorococcus* maintains the smallest genome (1.6-2.7 Mb) known for any free-living phototroph (15).

Typically, cyanobacteria harbor multiple iron uptake systems (16). Common is the use of organic ligands used to solubilize iron (siderophores) using the TonB transport system (17). The majority of the *Prochlorococcus* species lack genes for siderophore biosynthesis (18, 19); instead, the bacterium primarily relies on the Fut ABC transporter system for iron uptake (20). Here, specialized periplasmic iron binding proteins sequester elemental iron and deliver it to ABC transporters for uptake (16) that uses the FutA2 substrate binding protein (SBP) as a periplasmic ferric iron binding protein (21, 22). Functional assignment of the FutA1 homologue is binding of ferrous iron within the cytoplasm to protect the photosystem against oxidative stress (23-25); however, FutA1 has also been shown to bind ferric iron (21, 26). We have previously shown that the single FutA protein of the marine cyanobacterium *Trichodesmium* may indeed have dual localization and function (27), suggesting a single FutA protein can bind both ferric and ferrous iron species. Similarly, *Prochlorococcus* harbors a single *futA* gene (20). We wanted to understand whether a single FutA protein can bind both iron species, and how redox plasticity was structurally encoded.

It is challenging to obtain crystallographic models without alteration of the metal sites, since site-specific damage occurs extremely quickly and at very low doses (28), particularly for iron (29, 30). Indeed, the FutA structure determined from a conventional diffraction experiment on an X-ray home source reported here represented the photo-reduced, ferrous binding state, corroborated by spectroscopic evidence. A serial femtosecond crystallography approach (SFX) using an XFEL source and a complementary neutron diffraction approach were required to avoid the manifestations of X-ray induced photoreduction in order to determine the ferric state and give protonation states of iron coordinating amino acid side chains. Using a fixed-target silicon chip system for crystal delivery (31) at both synchrotron and XFEL radiation sources, we studied the transition between ferric to ferrous states at room temperature whilst making use of the effects of X-ray induced photoreduction, varying dose and time. The resulting protein structures support a dual binding mode for iron and give insight into protein adaptation to evolutionary pressures.

Results

The structure of FutA at room temperature (RT). The crystallographic X-ray structure of FutA was determined from a single crystal to 1.7 Å resolution, using a standard rotation protocol with the crystal in a sealed capillary at a home source setup (**Table S1**). Substrate binding domains such as FutA can be classified based on overall fold (32), and *Prochlorococcus* FutA classifies as "D type" substrate binding protein. The N-terminal (amino acids 1-98 and 232-280, light grey) and C-terminal domains (amino acids 99-231 and 281-314, dark grey) are highlighted in **Fig. 1A**.

The substrate-binding cleft bears the iron-binding site that is open to the surrounding solvent. The four tyrosine side chains of Tyr13 from N-terminal and Tyr143, Tyr199 and Tyr200 from C-terminal domains coordinate the iron, **Fig. 1B**, in this Class IV substrate binding protein (33). The trigonal bipyramidal coordination involves Tyr13, Tyr143 and Tyr200 to form the trigonal plane with iron at its center, while Tyr199 and a coordinating solvent molecule are the axial ligands.

Interestingly, the structure reveals a positioning of two arginine side chains, Arg103 and Arg203, in a second shell around the iron binding site, **Fig. 1C**. One might assume the tyrosine side chains are negatively charged tyrosinates, and arginine side chains would each provide a positive charge, the solvent molecule being either water or a hydroxyl ion. To understand the state of the bound iron, we used spectroscopy and went on to confirm the protonation state of surrounding amino acids side chains using a neutron diffraction experiment.

Determination of the ferric iron binding state by Electron Paramagnetic Resonance (EPR) spectroscopy. A refolding protocol in presence of iron sulfate was used to purify FutA. The burgundy red color of the purified protein that can readily be bleached by excess sodium dithionite likely resulted from the ligand to metal charge transfer (LMCT) bands between the tyrosinate residues coordinating the Fe^{3+} ion, **Fig. 2A**. The EPR spectrum taken in solution shows

153 a sharp signal at a g-value of 4.29, **Fig. 2B**. This signal is indicative of a $|\pm 3/2\rangle$ doublet from a $3d^5$,
154 high-spin (S = 5/2) isotropic system (E/D ≈ 1/3), consistent with an Fe^{3+} ion bound to FutA (34).
155 The weaker signals (g = 5.67, g = 7.90) derive from either $|\pm 1/2\rangle$ ground state transitions or from
156 $|\pm 3/2\rangle$ resonances from rhombic species of the ferric iron. However, given the very high transition
157 probabilities for the g = 4.29 signal compared to the lower transition probability for ground state or
158 anisotropic species, the latter resonances likely represent a significant fraction of the total spins in
159 the sample. Excess of sodium dithionite leads to the loss of the EPR signal, **Fig. 2B**. This could
160 result from loss of iron binding and reduction in solution, or reduction of ferric iron to a colorless
161 and $3d^6$ EPR-silent (probably S=2) ferrous state within the active site.

162 **Protonation state of iron coordinating residues as determined by neutron diffraction.** To
163 confirm the presence of tyrosinates in FutA we determined the crystallographic structure of FutA
164 by neutron diffraction to 2.1 Å resolution at RT (**Tables S1 & S2**). The neutron diffraction
165 structure shows that the side chain of Arg203 is not engaged in any interactions and does not
166 contribute to the second shell (**Fig. S1**), in contrast to the RT X-ray structure, **Fig. 1**. Positive
167 density in the neutron F_o-F_c omit map indicates sites of successful hydrogen-deuterium exchange,
168 revealing the fully protonated and thus positively charged side chain of Arg103, **Fig. 2C**. The lack
169 of deuterium on the iron coordinating Tyr13, Tyr143, Tyr199 and Tyr200 suggests these residues
170 are tyrosinates. Thus, the iron binding site is made up from four negatively charged tyrosinates
171 and a positively charged arginine in the second shell. Assuming the solvent molecule is neutral
172 water, iron bound in the ferric Fe^{3+} state would give charge balance.

173 **The ferric iron state structure determined by serial femtosecond crystallography (SFX).**
174 The SFX experiment used short (10 fs), high-intensity X-ray pulses from the SACLA XFEL to
175 provide diffraction patterns that are collected before the crystal is destroyed (35). It has been
176 shown that data can be recorded free of the effects of radiation induced changes as long as
177 sufficiently short pulses (<20 fs) are used (36). Crystallization conditions were optimized to obtain
178 microcrystal slurries suitable for SFX, as described by us previously (37). For data collection,
179 crystals of approximately 20 x 7 x 7 μm^3 were applied onto a fixed-target silicon chip, with the
180 final dataset merged from three chips (**Table S1**).

181 SFX and neutron diffraction structures are similar (see comparison in SI), with the Arg103 side
182 chain contributing to the second shell, but the side chain of Arg203 pointing away from the
183 binding site, **Fig. 2D**. EPR data, neutron diffraction and SFX agree and are consistent with iron
184 binding in the ferric state. In turn, this suggests that the structure determined from the RT X-ray
185 home source with the Arg203 side chain pointing towards the binding site as shown in **Fig. 1** may
186 represent the ferrous state.

187 **Characterization of X-ray induced photoreduction of ferric FutA.** The home source rotation
188 experiment might either fortuitously have captured the reduced state, or this observation had
189 resulted from X-ray induced photoreduction of Fe^{3+} to Fe^{2+}. Photoreduction was highly likely,
190 considering the bleaching of the burgundy-red appearance in the X-ray exposed area of the
191 crystal during data collection. We thus went on to characterize the effect of X-ray exposure using
192 *in crystallo* optical spectroscopy (38).

193 The electronic absorption peak (λ_{max} = 438 nm) corresponding to the ferric iron (39) progressively
194 decays on incident X-ray irradiation at a synchrotron beamline, **Fig. 3A**. As X-rays induce light-
195 absorbing chemical species in the solvent that overlap with the ferric iron specific signal, the 620
196 nm wavelength was chosen to minimize the effect of this artefact and characterize photoreduction
197 of the iron center, plotting absorbance against accumulated radiation dose, **Fig. 3B**. Measuring
198 five different crystals, we determined a half-photoreduction dose of 56 +/- 10 kGy; the dose at
199 which 80% of the molecules had been photoreduced was 90 +/- 13 kGy.

200 **Tracking of X-ray induced photoreduction from a dose series.** A fixed target dose slicing
201 approach with ten dose points at 10 ms exposure each was used to follow structural changes of

202 the FutA / iron complex in response to X-ray induced photoreduction (**Tables S3 & S4**). As
203 described by us previously (31)**,** serial synchrotron crystallography (SSX) was used as it is well
204 suited for low dose investigations at ambient temperatures, with the dose being spread across
205 thousands of crystals. The isomorphous difference density indicates an alternative conformation
206 for Arg203. The feature is readily visible at 22 kGy and strongest at 88 kGy, **Fig. 3C**. Indeed,
207 overlay with the conformation observed in the home source structure, **Fig. 1C**, shows that both
208 structures are similar, suggesting the photoreduced state was observed in both cases.

209 **An XFEL X-ray pump-probe (XRPP) approach capturing the transition between ferric and**
210 **ferrous states.** We designed a novel serial femtosecond crystallography experiment where a first
211 pulse, attenuated using a sapphire wafer mounted on a fast flipper, was followed by a second,
212 unattenuated pulse (**Fig. S2)**. Using SACLA's repetition rate of 30 Hz, the 10 fs pump and probe
213 were spaced 33 ms apart. While several different levels of attenuation were explored, data for a
214 500 kGy pump (94% attenuated) yielded structural changes consistent with photoreduction.
215 Interestingly, in contrast to the SSX series, **Fig. 3C**, this experiment preserves the iron
216 coordinating water that was clearly resolved in electron density, **Fig. 4**, consistent with penta-
217 coordinated ferrous iron. Ensuing refinement confirms presence of the alternative conformation of
218 Arg203 (**Fig. S3**). For the high occupancy state of Arg203 with the guanidino group closest to the
219 iron centre, distances were 4.8 Å between the η1 amide of Arg203 and the phenolate oxygen of
220 Tyr200, and 4.6 Å between the η2 amide of Arg203 and the alkoxy group of Tyr13. The XRPP
221 experiment thus induced specific alteration(s) and created the FutA ferrous state *in situ*.

222 **Discussion**

223 The adaptation of the marine cyanobacterium *Prochlorococcus marinus* is a remarkable story of
224 ecological success, making this photosynthetic organism the most abundant on earth. Two
225 factors are particularly important, the ability to survive under limiting nutrient conditions, and
226 physical size reduction, and both factors put evolutionary pressure on the iron uptake system of
227 the bacterium (13, 14). This study addresses the challenge of how a single gene product, FutA,
228 can bind both ferric and ferrous iron.

229 The structural analyses reported at ambient temperature allow delineating a plausible mechanism
230 for iron binding in two different oxidation states, showing how FutA Arg203 operates as a switch
231 between states. The side chain of this residue is not engaged in polar contacts in the ferric states,
232 which is hinting at its intrinsic dynamics, allowing it to be recruited and engage in interaction with
233 the iron center and contribute a balancing charge in the ferrous state, **Fig. 3D**.

234 X-ray crystallographic study of RedOx active metallo-proteins is challenging as X-ray induced
235 photoreduction can occur. Transition metals are particularly sensitive to specific radiation damage
236 (28, 40). Changes in the oxidation state induced by X-rays were previously documented for doses
237 as low as 33 kGy (30, 41). For Fe^{3+}, we show that the half-point for photoreduction corresponds
238 to a dose of 56 +/- 10 kGy, as shown by spectroscopic analysis, **Fig. 2B**. Observation of the FutA
239 ferrous state required SFX / neutron diffraction.

240 We exploited the effects of X-ray induced photoreduction to study the transition between ferric
241 and ferrous states, using a SSX dose series and an SFX X-ray pump probe setup, both allowing
242 to map conformational changes at ambient temperatures (42). The major difference observed
243 between these approaches occurred for density of the coordinating solvent water, which
244 disappeared with accumulating dose in SSX, **Fig. 3C**, while the SFX XRPP approach preserved
245 the electron density, **Fig. 4**. This may be attributed to the different time domains probed, or the
246 increasing non-isomorphousness in the SSX dose series (43, 44).

247 The dose delivered in a 10-femtosecond pulse in the SFX XRPP pump was with 500 kGy about
248 4.5-5.6 times higher than the doses used in the home source or SSX experiments, respectively.
249 However, the home source dataset required data collection for 1 hour, while the SSX dose series

was collected in 110 ms per crystal, and the SFX XRPP experiment was collected in 33 ms per crystal. Further to the different timescales, the SFX experiment used pulsed rather than continuous illumination, and/or could differ in heat load. Beam sizes were also different, with 10 micron for SSX and 1.5 micron for SFX experiments, providing an important difference for photo-electron escape (45). Further work is needed to understand radiation chemistry arising from these different conditions.

Discovery of a mechanism to bind two different iron oxidation states prompted us to revisit homologues of the FutA iron binding protein, and we found that a similar switch may exist for the iron binding protein FbpA from *Thermus thermophilus* with structures in two states reported (**Fig. S4**). *Synechocystis* has two specialized iron binding proteins (22, 26, 46), with FutA2 being assigned a ferric binding function in the oxidative environment of the periplasm, while FutA1 binds ferrous iron favored under reducing conditions in the cytosol. For these proteins, conservation of the arginine residue equivalent *Prochlorococcus* Arg203 (**Fig. S5**) may relate to biological ability to bind iron at different oxidation states, as discussed in supplementary text.

Conclusion: Structures with iron bound in different oxidation states help explain how the intrinsic structural plasticity of FutA accommodate ferrous as well as ferric iron species. Translated into a molecular mechanism, an arginine side chain flip provides a charge balance. The acute sensitivity of FutA to specific radiation damage illustrates the requirement for dose limiting data collection regimes. We have used photoreduction as an advantage to study the transition of ferric to ferrous binding state. The X-ray pump probe approach demonstrated here has the potential to become a straightforward-to-implement approach to induce redox state changes probing structural transitions. We envisage that more complex experiments could generate photoreduced states akin to anaerobic conditions that are amenable for further modification by ligand addition.

Materials and Methods

Molecular biology; *protein purification*; *protein crystallization*; *sample preparation for serial crystallography; crystallographic data processing; structure determination and refinement*; *processing of UV spectra* are found in Extended Materials and Methods in SI.

Dose calculations. Diffraction-weighted doses (DWD) as reported in all cases were calculated with *RADDOSE-3D* (47). For SFX XRPP, RADDOSE-3D rather than RADDOSE-XFEL was used as we were probing the effects of the total dose deposited by the pump pulse 33 milliseconds after the pulse rather than the time resolved evolution of dose within the duration of the pulse.

Home source crystal structure. RT data were collected from a single crystal grown from batch crystallization and measuring 0.32 x 0.53 x 0.54 mm^3, mounted in a 0.7 mm sealed quartz capillary on a Rigaku 007 HF (High Flux) diffractometer equipped with a HyPix 6000HE detector. The X-ray beam with a flux of 2.5 x 10^9 ph/s at 8.1 keV was collimated at 200 μm^2. The total exposure time of 1 hr equated to a total dose of 110 kGy.

Neutron crystallography. For hydrogen-deuterium exchange, FutA crystals grown from batch crystallization were transferred into crystal mother liquor prepared with deuterated water, in two subsequent exchanges for 24 hrs. Crystals with a volume larger than 0.2 mm^3 were mounted in 1 mm sealed quartz capillaries. Data collection at BIODIFF (48), Forschungsreaktor München II (Germany) used a monochromatic neutron beam. The final dataset was merged from two isomorphous crystals collected at wavelengths of 3.1023 and 3.0946 Å.

Serial synchrotron crystallography (SSX). SSX data were collected at beamline I24, Diamond Light Source, using silicon chips with 12 μm apertures. At each aperture ten images were collected to obtain two series with 5 kGy and 22 kGy dose-slicing (10 ms per image). Images were separated into individual dose points for processing (41). Datasets above a total dose of 110 kGy were no longer isomorphous with the lowest dose point, likely due to global damage, as

corroborated by the increase in B-factors, and tying with observation of difference density features “waning” at higher doses.

Serial femtosecond crystallography (SFX). SFX data were collected at SACLA beamline BL2 EH3, Japan, using the MPCCD detector. The XFEL was operated at an X-ray energy of 11.0 keV with a pulse length of 10 fs and a repetition rate of 30 Hz. Synchronizing chip translation with the XFEL pulse, data collection took roughly 14 mins per chip.

SFX X-ray pump probe. For the XRPP experiments, a flipper-attenuator was used to reduce the flux of alternate XFEL pulses. A fast, self-restoring rotary shutter (Branstrom Instruments, USA) mounted upstream of the sample and containing Sapphire wafer in a range of thicknesses was triggered, via TTL from a signal generator, to move the wafer into and out of the X ray beam path. Pump and probe diffraction images were separated based on total scattering intensity using the dxtbx.radial_average function from the DIALS software package (**Fig. S2**).

Electron paramagnetic resonance. FutA at a concentration of 50 μM was shock-frozen in liquid nitrogen. Data collection was carried out in EPR quartz tubes at liquid helium temperature. Reduction of FutA was carried out by addition of 500 μM sodium dithionite prior to freezing. X-band continuous wave EPR spectra were recorded on a Bruker eleXsys E500 spectrometer using a standard rectangular Bruker EPR cavity (ER4102T) equipped with an Oxford helium cryostat (ESR900). The spectrometer worked at X-band frequency with a 10 Gauss modulation amplitude and 2 mW microwave power. All spectra were recorded at 5 – 6 K.

RT in crystallo UV-vis absorption spectroscopy. X-ray dose dependent UV-vis absorption spectroscopy was performed at ESRF beamline BM07-FIP2 equipped with an online microspectrophotometer (38, 49). A 400 μm optical fibre was used to connect a balanced deuterium-halogen lamp (Mikropack DH2000-BAL, Ocean Optics) to the higher objective, while a 600 μm optical fibre connected the lower objective to a fixed-grating spectrophotometer equipped with a CCD detector (QE65 Pro, Ocean Optics). The focal volume probed by the microspectrophotometer of 50 x 50 x ~100 μm^3 was fully irradiated by the 200 x 200 μm^2 X-ray top-hat beam (flux between 4.1 and 5.0 x 10^{11} ph/s at 12.66 keV). Spectra were acquired at 0.4 Hz (250 ms acquisition time averaged 10 times). Crystals with a volume between 160 x 70 x 50 μm^3 and 200 x 90 x 80 μm^3 were oriented to optimize the signal-to-noise ratio of the spectra, and maintained still during X-ray exposure in a loop-mount using a humidity controller (HC-Lab, Arinax) (50).

Acknowledgments

We thank Chris Holes for macromolecular crystallization, Peter Horton for diffraction, and Peter Roach for critical discussion at the University of Southampton (UoS). We are grateful to SACLA beamline staff, in particular Shigeki Owada and Kensuke Tono for technical assistance. We acknowledge financial support: Biological Sciences Research Council (BBSRC) to the XFEL program under Japan Partnering Award BB/R021015/1 and BB/W001950/1; the Japan Synchrotron Radiation Research Institute 2018A8005 and 2019A8004; the UK XFEL Hub, Diamond Light Source (DLS) for travel support; studentship support by the South Coast Biosciences Doctoral Training Partnership (SoCoBio DTP) to JS, the National Oceanography Center to MoM, the DLS and UoS to RB, MoM, JS, MR, and Hamburg University to NC. UV-vis absorption spectroscopy experiments were carried out using the BM07-FIP2 and *ic*OS platforms of the Grenoble Instruct-ERIC Center (ISBG; 404 UAR 3518 CNRS-CEA-UGA-EMBL) within the Grenoble Partnership for Structural Biology supported by FRISBI (ANR-10-INBS-0005-02) and the University Grenoble Alpes graduate school supported by CBH-EUR-GS (ANR-17-EURE-0003), carried out in the RADDAM bag. AMO and JS were supported in part by DLS, the UK Science and Technology Facilities Council, the BBSRC, the Wellcome Investigator Award 210734/Z/18/Z, and a Royal Society Wolfson Fellowship RSWF\R2\182017 (all to AMO).

References

1. K. Hans Wedepohl, The composition of the continental crust. *Geochimica et Cosmochimica Acta* **59**, 1217-1232 (1995).
2. P. W. Boyd *et al.*, Mesoscale Iron Enrichment Experiments 1993-2005: Synthesis and Future Directions. *Science* **315**, 612-617 (2007).
3. M. L. Wells, N. M. Price, K. W. Bruland, Iron chemistry in seawater and its relationship to phytoplankton: a workshop report. *Marine Chemistry* **48**, 157-182 (1995).
4. W. Stumm, B. Sulzberger, The cycling of iron in natural environments: Considerations based on laboratory studies of heterogeneous redox processes. *Geochimica et Cosmochimica Acta* **56**, 3233-3257 (1992).
5. H. W. Rich, F. M. M. Morel, Availability of well-defined iron colloids to the marine diatom Thalassiosira weissflogii. *Limnology and Oceanography* **35**, 652-662 (1990).
6. J. A. Raven, M. C. W. Evans, R. E. Korb, The role of trace metals in photosynthetic electron transport in O2-evolving organisms. *Photosynthesis Research* **60**, 111-150 (1999).
7. S. Richier *et al.*, Abundances of Iron-Binding Photosynthetic and Nitrogen-Fixing Proteins of Trichodesmium Both in Culture and In Situ from the North Atlantic. *PLoS ONE* **7**, e35571 (2012).
8. J. T. Snow *et al.*, Quantifying Integrated Proteomic Responses to Iron Stress in the Globally Important Marine Diazotroph Trichodesmium. *PLOS ONE* **10**, e0142626 (2015).
9. Z. S. Kolber *et al.*, Iron limitation of phytoplankton photosynthesis in the equatorial Pacific Ocean. *Nature* **371**, 145-149 (1994).
10. M. C. Moore *et al.*, Large-scale distribution of Atlantic nitrogen fixation controlled by iron availability. *Nature Geoscience* **2**, 867-871 (2009).
11. M. A. Huston, S. Wolverton, The global distribution of net primary production: resolving the paradox. *Ecological Monographs* **79**, 343-377 (2009).
12. P. Flombaum *et al.*, Present and future global distributions of the marine cyanobacteria Prochlorococcus and Synechococcus. *Proceedings of the National Academy of Sciences* **110**, 9824-9829 (2013).
13. S. J. Biller, P. M. Berube, D. Lindell, S. W. Chisholm, Prochlorococcus: the structure and function of collective diversity. *Nature Reviews Microbiology* **13**, 13-27 (2015).
14. F. Partensky, W. R. Hess, D. Vaulot, Prochlorococcus, a Marine Photosynthetic Prokaryote of Global Significance. *Microbiology and Molecular Biology Reviews* **63**, 106-127 (1999).
15. P. M. Berube *et al.*, Single cell genomes of Prochlorococcus, Synechococcus, and sympatric microbes from diverse marine environments. *Sci Data* **5**, 180154 (2018).
16. R. Sutak, J.-M. Camadro, E. Lesuisse, Iron Uptake Mechanisms in Marine Phytoplankton. *Frontiers in Microbiology* **11** (2020).
17. M. Sandy, A. Butler, Microbial Iron Acquisition: Marine and Terrestrial Siderophores. *Chem Rev* **109**, 4580-4595 (2009).
18. D. B. Rusch, A. C. Martiny, C. L. Dupont, A. L. Halpern, J. C. Venter, Characterization of Prochlorococcus clades from iron-depleted oceanic regions. *Proceedings of the National Academy of Sciences* **107**, 16184-16189 (2010).
19. R. R. Malmstrom *et al.*, Ecology of uncultured Prochlorococcus clades revealed through single-cell genomics and biogeographic analysis. *International Society for Microbial Ecology Journal* **7**, 184-198 (2013).
20. G. Rocap *et al.*, Genome divergence in two Prochlorococcus ecotypes reflects oceanic niche differentiation. *Nature* **424**, 1042-1047 (2003).
21. H. Katoh, N. Hagino, A. R. Grossman, T. Ogawa, Genes essential to iron transport in the cyanobacterium Synechocystis sp. strain PCC 6803. *Journal of Bacteriology* **183**, 2779-2784 (2001).
22. A. Badarau *et al.*, FutA2 is a ferric binding protein from Synechocystis PCC 6803. *Journal of Biological Chemistry* **283**, 12520-12527 (2007).

23. P. Exss-Sonne, J. Tölle, K. P. Bader, E. K. Pistorius, K.-P. Michel, The IdiA protein of Synechococcus sp. PCC 7942 functions in protecting the acceptor side of Photosystem II under oxidative stress. *Photosynthesis Research* **63**, 145-157 (2000).
24. J. Tölle *et al.*, Localization and function of the IdiA homologue Slr1295 in the cyanobacterium Synechocystis sp. strain PCC 6803. *Microbiology* **148**, 3293-3305 (2002).
25. K. P. Michel, E. K. Pistorius, Adaptation of the photosynthetic electron transport chain in cyanobacteria to iron deficiency: The function of IdiA and IsiA. *Physiologia Plantarum* **120**, 36-50 (2004).
26. H. Katoh, N. Hagino, T. Ogawa, Iron-binding activity of FutA1 subunit of an ABC-type iron transporter in the cyanobacterium Synechocystis sp. Strain PCC 6803. *Plant and Cell Physiology* **42**, 823-827 (2001).
27. D. Polyviou *et al.*, Structural and functional characterization of IdiA/FutA (Tery_3377), an iron-binding protein from the ocean diazotroph Trichodesmium erythraeum. *Journal of Biological Chemistry* **293**, 18099-18109 (2018).
28. E. F. Garman, M. Weik, Radiation Damage in Macromolecular Crystallography. *Methods Mol Biol* **1607**, 467-489 (2017).
29. J. A. R. Worrall, M. A. Hough, Serial femtosecond crystallography approaches to understanding catalysis in iron enzymes. *Curr Opin Struc Biol* **77** (2022).
30. V. Pfanzagl *et al.*, X-ray–induced photoreduction of heme metal centers rapidly induces active-site perturbations in a protein-independent manner. *Journal of Biological Chemistry* **295**, 13488-13501 (2020).
31. S. Horrell *et al.*, Fixed Target Serial Data Collection at Diamond Light Source. *J Vis Exp* 10.3791/62200 (2021).
32. G. H. Scheepers, J. A. Lycklama A Nijeholt, B. Poolman, An updated structural classification of substrate-binding proteins. *Federation of European Biochemical Societies Letters* **590**, 4393-4401 (2016).
33. S. Wang *et al.*, A novel mode of ferric ion coordination by the periplasmic ferric ion-binding subunit FbpA of an ABC-type iron transporter from Thermus thermophilus HB8. *Acta Crystallographica Section D* **70**, 196-202 (2014).
34. G. Palmer, The electron paramagnetic resonance of metalloproteins. *Biochem Soc Trans* **13**, 548-560 (1985).
35. H. N. Chapman, X-Ray Free-Electron Lasers for the Structure and Dynamics of Macromolecules. *Annu Rev Biochem* **88**, 35-58 (2019).
36. K. Nass *et al.*, Structural dynamics in proteins induced by and probed with X-ray free-electron laser pulses. *Nat Commun* **11**, 1814 (2020).
37. J. H. Beale *et al.*, Successful sample preparation for serial crystallography experiments. *Journal of Applied Crystallography* **52**, 1385-1396 (2019).
38. D. von Stetten *et al.*, In crystallo optical spectroscopy (icOS) as a complementary tool on the macromolecular crystallography beamlines of the ESRF. *Acta Crystallogr D Biol Crystallogr* **71**, 15-26 (2015).
39. A. M. Orville, N. Elango, J. D. Lipscomb, D. H. Ohlendorf, Structures of competitive inhibitor complexes of protocatechuate 3,4-dioxygenase: multiple exogenous ligand binding orientations within the active site. *Biochemistry* **36**, 10039-10051 (1997).
40. M. A. Hough, R. L. Owen, Serial synchrotron and XFEL crystallography for studies of metalloprotein catalysis. *Curr Opin Struct Biol* **71**, 232-238 (2021).
41. A. Ebrahim *et al.*, Dose-resolved serial synchrotron and XFEL structures of radiation-sensitive metalloproteins. *International Union of Crystallography Journal* **6**, 543-551 (2019).
42. J. S. Fraser *et al.*, Accessing protein conformational ensembles using room-temperature X-ray crystallography. *Proc Natl Acad Sci U S A* **108**, 16247-16252 (2011).
43. G. Gotthard *et al.*, Specific radiation damage is a lesser concern at room temperature. *International Union of Crystallography Journal* **6**, 665-680 (2019).

44. E. De La Mora *et al.*, Radiation damage and dose limits in serial synchrotron crystallography at cryo- and room temperatures. *Proceedings of the National Academy of Sciences* **117**, 4142-4151 (2020).
45. S. L. S. Storm *et al.*, Measuring energy-dependent photoelectron escape in microcrystals. *IUCrJ* **7**, 129-135 (2020).
46. N. Koropatkin, A. M. Randich, M. Bhattacharyya-Pakrasi, H. B. Pakrasi, T. J. Smith, The structure of the iron-binding protein, FutA1 from Synechocystis 6803. *Journal of Biological Chemistry* **282**, 27468-27477 (2007).
47. C. S. Bury, J. C. Brooks-Bartlett, S. P. Walsh, E. F. Garman, Estimate your dose: RADDOSE-3D. *Protein Science* **27**, 217-228 (2018).
48. T. S. A. Ostermann, BIODIFF: Diffractometer for large unit cells. *Journal of large-scale research facilities* **1**, A2 (2015).
49. J. McGeehan *et al.*, Colouring cryo-cooled crystals: online microspectrophotometry. *J Synchrotron Radiat* **16**, 163-172 (2009).
50. J. Sanchez-Weatherby *et al.*, Improving diffraction by humidity control: a novel device compatible with X-ray beamlines. *Acta Crystallogr D Biol Crystallogr* **65**, 1237-1246 (2009).

Figures and Tables

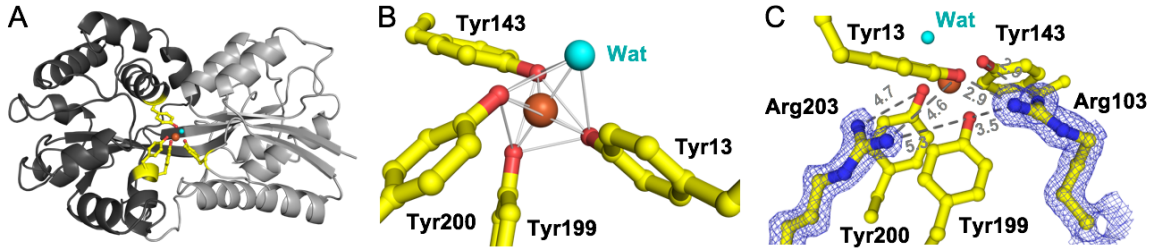

Figure 1. The FutA structure (ferrous state) from an X-ray home source determined to 1.7 Å resolution at room temperature. (*A*) FutA has a bi-lobal structure with the substrate binding cleft between the N-terminal (light grey) and C-terminal domains (dark grey). Amino acid side chains contributing to iron binding are shown in stick representation (yellow). (*B*) Trigonal bipyramidal coordination of the iron, with Tyr199 and a solvent molecule as axial ligands. (*C*) The two arginine side chains of Arg103 and Arg203 are in a second coordination shell, shown here with refined density (blue map, contoured at 1.5 σ). Color coding is yellow for carbon, red for oxygen, blue for nitrogen, orange for iron, with the solvent water in light blue.

Figure 2. FutA (ferric state) characterized by UV/Vis and EPR spectroscopy, neutron diffraction and serial femtosecond crystallography. (*A*) The UV-vis spectrum of recombinantly produced and purified FutA (blue) shows an absorbance maximum at 438 nm, consistent with ferric bound to FutA. The peak at 438 nm disappears after addition of 10-fold molar excess sodium dithionite (yellow), where the absorbance maximum of 315 nm resulted from free sodium dithionite. (*B*) EPR spectrum of the FutA iron complex, and a sodium dithionite reduced sample. The peaks observed were: g1 = 4.29 g, g2 = 5.67 g, g3 = 7.9 g. (*C*) Iron binding site in the neutron diffraction crystal structure. The positive neutron density (green mesh, $F_{obs} - F_{calc}$ omit map at 3σ, 2.1 Å resolution) indicates sites that have undergone hydrogen-deuterium exchange and suggesting Arg103 is positively charged. The four tyrosine side chains do not show difference density, suggesting they are negatively charged tyrosinates. (*D*) The structure determined by SFX resolves the side chain of Arg103 in the second shell. However, the side chain of Arg203 is not oriented towards the binding site and does not engage in polar interactions (similar to neutron diffraction structure **Fig. S1**). Carbons shown blue (neutron diffraction) or green (SFX), heteroatoms colored as in **Fig. 1**.

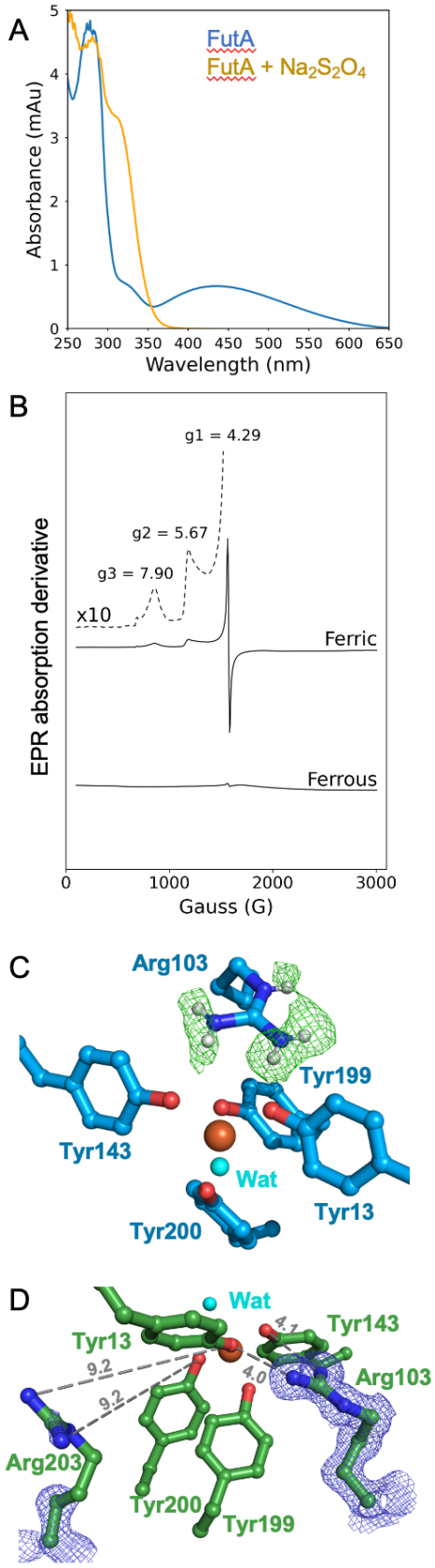

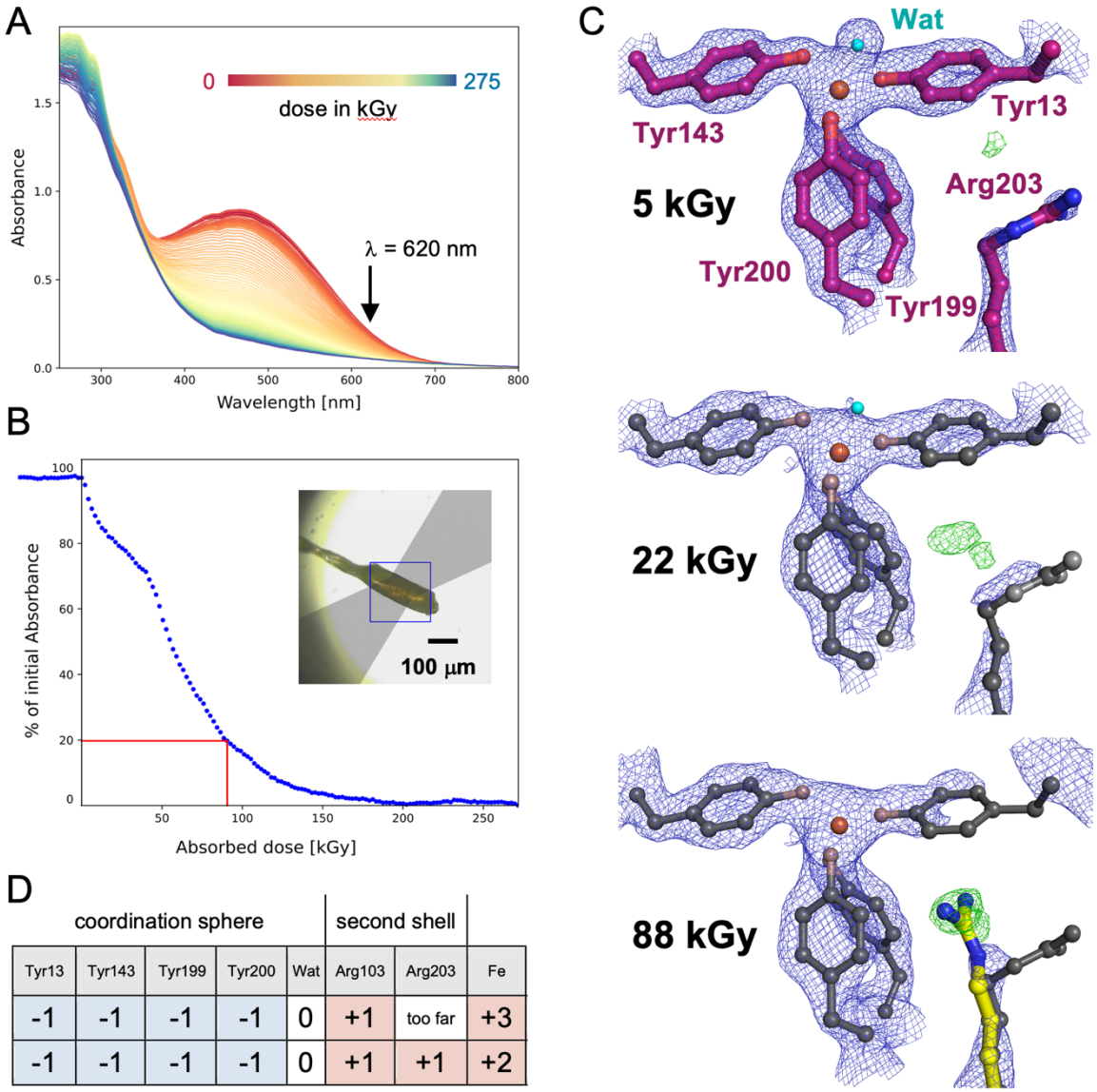

D

coordination sphere					second shell		
Tyr13	Tyr143	Tyr199	Tyr200	Wat	Arg103	Arg203	Fe
-1	-1	-1	-1	0	+1	too far	+3
-1	-1	-1	-1	0	+1	+1	+2

Figure 3. X-ray induced photoreduction of FutA characterized by spectroscopy and SSX at RT. (*A*) Successive UV-Vis absorption spectra collected *in crystallo* plotted for a FutA crystal during X-ray exposure, from 0 kGy (red) to 275 kGy (blue). Photoreduction was monitored at a wavelength of 620 nm (arrow). (*B*) Evolution of the normalized absorbance at 620 nm, collected on a single crystal. In the example shown, 80% of the signal was lost at 91 kGy (red lines). Inset: geometry of the experiment; the X-ray beamsize of 200 μm^2 was matched to the crystal (215 µm in the longest dimension; the light path for spectroscopy is indicated (focal spot 100 µm in diameter, light path indicated in grey). (*C*) SSX dose series at RT. Top: refined structure at 5 kGy (carbon atoms shown in purple; 2Fo-Fc density in blue contoured at 1.5 σ, Fo-Fc in green contoured at 3 σ). Pronounced difference density is seen at 22 kGy and 88 kGy, suggesting Arg203 takes an alternative conformation, as indicated by overlay with the conformation seen in the ferrous state determined from the home source (Arg203 carbons shown in yellow for the 88 kGy dose point). Heteroatoms colored as in **Fig. 1**. (*D*) Charges of amino acids contributing to the coordination sphere and second shell for the Fe^{3+} ferric and Fe^{2+} ferrous binding states, assuming an overall neutral state of the binding site.

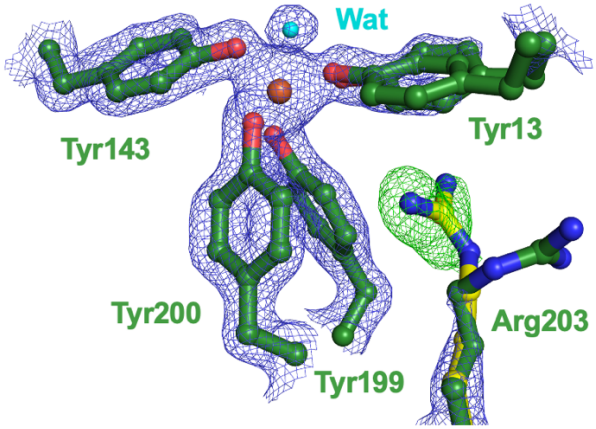

Figure 4. SFX X-ray pump probe experiment. The model of the ferric iron state determined SFX (compare **Fig. 2D**) was used in refinement against an SFX probe dataset, collected after a 500 kGy pump, in which the side chain of Arg203 was modelled as observed in the ground state structure. Refined electron density shows Tyr13 in a double conformation and limited density for the Arg203 guanidino group (2Fo-Fc, blue, 1.5 σ). However, difference density (Fo-Fc, green, 3 σ) suggests that Arg203 takes an alternative conformation, indicated by overlay with the conformation seen in the ferrous state determined from the home source (Arg203 carbons shown in yellow). Heteroatoms colored as in **Fig. 1**.

Supplement for

A redox switch allows binding of ferrous and ferric ions in the cyanobacterial iron binding protein FutA from *Prochlorococcus*

Rachel Bolton *et al.*

This supplement includes:

Extended Materials and Methods
Supplementary Text
Tables S1 to S4
Figures S1 to S5

Extended Materials and Methods

Molecular biology. Prochlorococcus MED4 *futA* was cloned into pET-24b(+) using the NdeI / HindIII restriction sites, excluding the region encoding the signal peptide, amino acids 27-340 (UniProt ID: Q7V0T9) as predicted by *SignalP* (1).

Protein purification. Transformed *Escherichia coli* BL21 (DE3) cells (NEB) were cultured in 3 L baffled flasks in 1 L lysogeny broth containing 50 μg ml^{-1} kanamycin, and incubated in a shaker at 130 RPM, 37 °C. The temperature was reduced to 18 °C when the cell culture reached an OD_{600} of 0.4. Protein expression was induced at an OD_{600} of ~0.6 by addition of IPTG (final concentration 1 mM). Cells were harvested after 20 hrs by centrifugation at 4000 x g (Avanti Jxn-26, JLA-8.1000 rotor). Cell pellets (2-4g) were resuspended in 25 ml IBB buffer (0.1 M Tris buffered at pH 9, containing 0.5 M NaCl, 1% Triton-X, 5 mM $MgCl_2$ and 10 mM β-mercaptoethanol). For lysis 2 mg ml^{-1} lysozyme was added, and cells were left for 30 min before sonication for total pulse time of 150 seconds (Q700 Sonicator, 10 second pulse duration with 20 seconds between pulses). Inclusion bodies were harvested by centrifugation (40 mins, 125 000 x g, 4 °C, Optima XPN-80, Type 70 Ti rotor). The pellet was washed in IBB containing 2 M urea, followed by centrifugation (as above). Solubilization was carried out by incubation in 200 mM Tris buffered at pH 9, containing 6 M urea, 10 mM β-mercaptoethanol (1 hrs, 4 °C). After removing cellular debris by centrifugation (as above), a rapid dilution protocol was carried out to refold the protein. The salute was loaded into a syringe with a fine needle and slowly added directly into 2 L of stirring 0.2 M Tris buffered at pH 9.0, containing 0.2 M NaCl, 0.4 M L-Arginine and 0.1 mM $NH_4Fe(SO_4)_2$. After incubation at 4 °C for 48 h, the refolding buffer was concentrated to 150 ml using an Amicon Stirred Cell (10,000 Da Ultrafiltration Disk, Merck). Dialysis against 2 L 100 mM Tris buffered at pH 9.0, containing 145 mM NaCl for 24 hrs at 4 °C was followed by capture on a 5 ml HiTrap SP XL column (GE Healthcare) at RT. Step-elution with 0.1 M Tris buffered at pH 9.0, containing 320 mM NaCl was followed by size-exclusion chromatography on a HiLoad 16/60 Superdex 200 column (GE Healthcare) using 50 mM Tris buffered at pH 9.0, containing 300 mM NaCl at RT. Fractions containing monomeric FutA were pooled and concentrated using a Vivaspin 20 Centrifugal Concentrator, MWCO 10,000 Da (Sartorius) at 4 °C.

Protein Crystallization. FutA at a concentration of ~50 mg ml^{-1} was crystallized at RT at the natural pH from purification (pH 9.0). For <u>vapor diffusion crystallization</u>, 1 μl protein was mixed with 1 μl 0.2 M sodium thiocyanate containing 10 - 35 % (w/v) PEG 3350 and set up in 24-well XRL plates (Molecular Dimensions). Crystals with 10 – 200 μm in the longest dimension appeared within 1 day. For <u>batch crystallization</u>, 10 μl of protein was mixed in a microcentrifuge tube with 10 μl of 0.2 M sodium thiocyanate containing 10 - 24 % (w/v) PEG 3350. Crystals with 200 – 1500 μm in the longest dimension appeared within 3 days. For <u>seeded batch crystallization</u>, 10 μl of FutA crystals obtained from vapor diffusion droplets were mixed with 40 μl 20% PEG 3350 and vortexed with Hampton Seed Bead for 180 s. Seed stock aliquots (5 μl) were shock frozen and diluted 1:100 with 0.2 M sodium thiocyanate, 20 % (w/v) PEG 3350 prior to use. For crystallization, 50 μl protein was mixed with 75 μl diluted seed stock and 75 μl of 0.2 M sodium thiocyanate containing 10 - 20 % (w/v) PEG 3350. Crystals with 10 – 20 μm in the longest dimension appeared within 30 minutes as described previously (2).

Sample preparation for serial crystallography. Optimization of crystallization for serial crystallography was described previously (2). We used a fixed-target silicon chip, each accommodating 25,600 apertures, to deliver microcrystals to the X-ray interaction region (3). The crystal slurry (typically 150 μl) was loaded onto a glow-discharged chip containing 7 or 12 μm sized apertures within a humidity-controlled chamber, collected by applying vacuum, and sealing the chip between two sheets of 6 μm thick Mylar. Crystal slurries had to be prepared directly before the experiment to avoid crystal ageing that manifested as loss of diffraction.

Crystallographic data processing, structure determination and refinement. The <u>home source diffraction data</u> were integrated with *XDS* (4), and scaled / merged using *POINTLESS* and

AIMLESS (5). The Neutron diffraction data were integrated using *HKL2000* (6) and scaled / merged using *SCALEPACK* (6). The diffraction data for the SSX dose series was indexed and integrated using *dials.stills_process* (*DIALS* v2.0) (7) and scaled using *cctbx.prime* (8). Results for two dose-series are shown in **Table S2**, using 5 kGy and 22 kGy dose-slicing. B-factor sharpening was applied in scaling to correct for the increase in B-factors in each series. *SCALEit* (9) was used to derive the isomorphous difference between two datasets (D_{iso}), and scale the differences in observed structure factors between datasets. SFX diffraction data were stored in a hdf5 stream, applying indexing and pre-filtering for diffraction hits with *Cheetah* (10). Diffraction hits were indexed and integrated with *dials.stills_process* (*DIALS* v3.0) (7). An image mask was generated manually using *dials.image_viewer* to remove the beam stop shadow and monocrystalline Si diffraction spots arising from the chips. Integrated patterns were scaled and merged using the *DIALS* module *cctbx.xfel.merge* (11). Molecular replacement with *MOLREP* (12) used the *Synechocystis* PCC 6803 FutA2 as search model (PDB: 2PT1). *COOT* (13), and *REFMAC5* (14) were used for iterative model building, refinement and validation. Coordinates and structure factors were deposited with the PDB under accession numbers 8OEM (Home Source), 8OEN (Neutron), 8C4Y (SFX), 8OGG (SSX 5 kGy), and 8OEI (SFX 500kGy), using the EBI validation suite.

Processing and plotting of online UV-Vis spectra was performed in Python with the *NumPy* (15), *pandas* (16), *SciPy* (17), *statsmodels* (18) and *Matplotlib* (19) packages. Each spectrum was smoothed using a Savitzky-Golay filter (filter order 3, filter length 25). Baseline correction used subtraction of the average absorbance calculated between 800 and 880 nm.

Supplementary Text

Comparison of neutron diffraction and SFX structures

Further investigation of the iron binding site was carried out by comparing the SFX model and neutron diffraction model. Refinement of structures obtained by neutron macromolecular crystallography (NMX) was carried out with the procedures as implemented by us in REFMAC5, available through CCP4 v8.0.

We tested two different strategies to refine the iron binding site:

1. Refinement with "`no link`" restraints between the OH of the iron coordinating tyrosinates Tyr13, Tyr143, Tyr 199 and Tyr200, or the proximal solvent water molecule.
2. Using link restraints between for the above interaction partners, generated as ideal values for an Fe-O link as derived from the Crystallography Open Database (COD) (20). Link dictionaries used ideal values of 1.8 Å for the equatorial and 2.004 Å for the axial ligands, respectively.

We compare the "`no link`" restraint refinement with results from four different sigma values as applied with the Fe-O link restraints. The observed distances after refinement after refinement for both SFX and NMX models are reported in **Table S2**. The comparison showed that distances converged in SFX, while in NMX distances were biased towards restraint target values, as evident when higher sigma levels were applied. The distance to the axial solvent ligand was larger in NMX than in SFX structures, leading to a distorted tetrahedron.

Analysis of sequence conservation in the iron binding site of FutA proteins

The data in this manuscript suggest that *Prochlorococcus* MED4 FutA can bind iron in the ferric and in the ferrous redox states, using an arginine switch mechanism. This observation raises the question whether this concept can be extended to other FutA homologues. We therefore carried out multiple sequence alignment analysis (MSA) across a set of known FutA homologues, **Fig. S5**.

The bacterial species selected here are gram-negative, free-living marine bacteria that are found in oligotrophic ocean waters. Of these, *Prochlorococcus* MED4 and *Synechocystis* PCC 6803 are capable of carbon fixation, whereas *T. erythraeum* and *C. chwakensis* are also capable of nitrogen fixation. *T. thermophilus* is a heterotrophic, extremophile, isolated from deep-sea thermal vents. Species with a single FutA homologue in their genome were *Prochlorococcus* MED4 (UniProt ID: Q7V0T9), *Trichodesmium erythraeum* (UniProt ID: Q10Z45), *Crocosphaera chwakensis* (A3IPT8), and *Thermus thermophilus* (UniProt ID: Q5SHV2). In contrast, *Synechocystis* PCC 6803 has two FutA homologies, denoted as FutA1 (UniProt ID: P72827) and FutA2 (UniProt ID: Q55835).

The sequences of the FutA homologues were aligned with Clustal Omega (21) and visualized with JalView (22), as shown in **Fig. S5**. Conservation is shown in blue and indicates the conservation of the physio-chemical properties of the amino acids across the sequence alignment (22).

For species encoding a single FutA protein the arginine residue equivalent to Arg203 in *Prochlorococcus* MED4 FutA was conserved. Interestingly, this amino acid is even conserved *Synechocystis* PCC 6803 which has two FutA homologues, which may suggest that FutA1 and FutA2 both have capacity to bind ferric or ferrous iron. This observation aligns with gene knockout studies conducted by us (23) demonstrating a degree of redundancy between the two FutA homologues.

The iron binding site in FpbA from *T. thermophilus* differs from the other proteins, as the residues equivalent to *Prochlorococcus* MED4 FutA His12 and Tyr13 are exchanged to Glycine and Glutamine, respectively. Despite this, the residue equivalent to Arg203 is conserved (Arg223). As FbpA switches from an open (PDB: 3WAE) to a closed conformation (PDB: 4ELR) upon iron binding, a carbonate ion is lost from the binding site and Arg223 is repositioned away from the binding site, **Fig. S4** (24, 25). This ability of Arg223 to act as a structural switch and maintain a net neutral charge in the binding site is therefore highly similar to the observed structural rearrangement of Arg203 in *Prochlorococcus* MED4 FutA.

Table S1. Data collection and refinement statistics for FutA structures reported in space group $P2_1$.

Data collection statistics

	Home Source	Neutron	SFX	SSX 5 kGy	SFX 500kGy
Temperature (°C)	21	21	25	21	25
Wavelength	1.54	3.10	1.13	0.97	1.13
# Integrated Lattices			78743	5,278	24,378
# Merged Lattices			77936	5,170	24,141
Unit Cell (a, b, c; Å)	39.4, 78.0, 48.0	39.5, 78.3, 47.9	39.1, 78.3, 47.4	39.7, 78.7, 48.4	39.4, 78.2, 48.0
β angle (°)	98.2	97.4	97.4	97.8	97.9
Resolution (all, Å)	47.50 – 1.70	24.95 – 2.1	30.10 – 1.60	40.97 – 1.76	32.42 – 1.65
Resolution (HR, Å)	1.73 – 1.70	2.18 – 2.1	1.63 – 1.60	1.79 – 1.76	1.68 – 1.65
R_{split} / R_{pim}[1]	0.009 (0.089)	0.098 (0.332)	0.053 (0.089)	0.235 (0.684)	0.134 (0.691)
CC ½ (%)[1]	100.0 (98.6)	97.1 (68.1)	99.6 (90.6)	92.3 (43.1)	97.0 (40.0)
$I/\sigma I$[1]	71.7 (11.6)	4.8 (2.0)	12.1 (4.6)	3.14 (0.41)	3.67 (0.43)
Completeness (%)[1]	97.9 (83.5)	81.0 (52.6)	99.8 (100.0)	100.0 (100.0)	100.0 (100.0)
Multiplicity[1]	65.4 (42.1)	1.9 (1.1)	618.7 (274.5)	26.2 (19.1)	165.2 (82.4)
Unique Reflections[1]	30,881 (1,369)	13,731 (890)	37,266 (1,877)	29,256 (1,467)	34,653 (1676)
Wilson B-factor (Å^2)	14.10	10.07	12.09	24.28	20.98

Refinement statistics

	Home Source yellow	Neutron blue	SFX green	SSX 5 kGy purple	SFX 500 kGy green
PDB Code	8OEM	8OEN	8C4Y	8OGG	8OEI
Resolution (Å)	47.50 – 1.70	24.95 – 2.1	30.10 – 1.60	40.97 – 1.76	32.42 – 1.65
Rwork/Rfree	0.153 / 0.180	0.182 / 0.250	0.190 / 0.208	0.202 / 0.241	0.162 / 0.189
# Reflections all/free	30847 / 1,588	13,731 / 698	37,266 /1919	29256 / 1503	34653 / 1786
Number of Atoms					
Protein	2558	4984	2485	2509	2572
Ion	1	1	1	1	1
Water	117	81	86	81	105
Ramachandran					
Preferred	305	298	304	301	302
Allowed	4	11	5	8	7
Outliers	1	1	1	1	1
B-factors (Å^2)					
Protein	19.71	22.31	17.84	33.32	27.06
Water	25.32	13.41	23.32	48.19	33.05
R.M.S Deviations					
Bond Lengths (Å)	0.013	0.005	0.013	0.006	0.009
Bond Angles (°)	1.88	1.14	1.76	1.41	1.54

[1]High resolution statistics in parentheses

Table S2. Comparison of different types of refinement for SFX and NMX structures. Bond lengths between Fe and the hydroxyl group of the tyrosinates as well as the proximal water. All tabulated bond lengths are in Å.

SFX	no link	Fe-Tyr link (1.8 Å)				Fe-Tyr link (2.004 Å)			
Fe-O		0.01 σ	0.02 σ	0.03 σ	0.04 σ	0.01 σ	0.02 σ	0.03 σ	0.04 σ
Fe-Tyr13	1.80	1.80	1.80	1.80	1.80	1.94	1.86	1.83	1.82
Fe-Tyr143	1.97	1.87	1.93	1.95	1.96	1.99	1.98	1.98	1.98
Fe-Tyr199	1.87	1.83	1.85	1.86	1.87	1.95	1.91	1.89	1.89
Fe-Tyr200	1.82	1.81	1.82	1.82	1.82	1.93	1.87	1.84	1.83
Fe-Water	2.17	2.16	2.16	2.16	2.16	2.16	2.16	2.16	2.16
NMX									
Fe-Tyr13	2.09	1.81	1.85	1.90	1.95	2.01	2.02	2.04	2.05
Fe-Tyr143	1.95	1.81	1.83	1.85	1.87	2.0	2.0	1.99	1.99
Fe-Tyr199	1.83	1.80	1.80	1.80	1.81	2.0	1.98	1.96	1.94
Fe-Tyr200	1.91	1.81	1.83	1.85	1.87	2.0	1.99	1.98	1.97
Fe-Water	2.72	2.64	2.66	2.68	2.69	2.60	2.61	2.63	2.64

141 **Table S3**. Full data collection and refinement statistics for two SSX dose series reported in space group $P2_1$ Data collection was carried out at RT
142 (21 °C) at an energy of X-ray Energy of 12.8 keV for 10 consecutive exposures to give dose points at 5 kGy interval.

143

Data collection statistics for the 5 kGy SSX dose-series

Data Collection	**5 kGy**	**10 kGy**	**15 kGy**	**20 kGy**	**25 kGy**
Number of Integrated Lattices	5278	5089	5197	5158	5227
Number of Merged Lattices	5170	4984	4916	4946	4999
Unit Cell a, b, c (Å)	39.7, 78.7, 48.4	39.7, 78.7, 48.4	39.7, 78.7, 48.4	39.7, 78.7, 48.4	39.7, 78.7, 48.4
β (°)	97.8	97.8	97.8	97.8	97.8
Resolution, overall (Å)	40.97 – 1.76	40.97 – 1.76	40.97 – 1.76	40.97 – 1.76	40.97 – 1.76
Resolution, high (Å)	1.79 – 1.76	1.79 – 1.76	1.79 – 1.76	1.79 – 1.76	1.79 – 1.76
R_{split}[1]	23.5 (68.4)	25.1 (70.8)	20.6 (95.8)	24.9 (71.8)	24.3 (72.8)
CC ½ (%)[1]	92.3 (43.1)	91.0 (38.5)	91.0 (38.9)	89.8 (41.4)	90.7 (42.5)
$I/\sigma I$[1]	3.14 (0.41)	3.24 (0.41)	3.29 (0.42)	3.33 (0.41)	3.39 (0.40)
Completeness (%)[1]	100.0 (100.0)	100.0 (100.0)	100.0 (100.0)	100.0 (100.0)	100.0 (100.0)
Multiplicity[1]	26.2 (19.1)	25.8 (18.8)	25.7 (18.8)	25.5 (18.6)	26.1 (19.0)
Unique Reflections[1]	29256 (1467)	29256 (1469)	29257 (1472)	29258 (1471)	29258 (1476)
Wilson B-factor ($Å^2$)	24.25	24.73	24.93	25.17	25.52

Data Collection	**30 kGy**	**35 kGy**	**40 kGy**	**45 kGy**	**50 kGy**
Number of Integrated Lattices	5372	5397	5410	5444	5400
Number of Merged Lattices	5119	5110	5115	5160	5147
Unit Cell a, b, c (Å)	39.7, 78.7, 48.4	39.7, 78.7, 48.4	39.7, 78.7, 48.4	39.7, 78.7, 48.4	39.7, 78.8, 48.4
β (°)	97.8	97.8	97.8	97.8	97.7
Resolution, overall (Å)	40.97 – 1.76	40.97 – 1.76	40.97 – 1.76	40.97 – 1.76	40.97 – 1.76
Resolution, high (Å)	1.79 – 1.76	1.79 – 1.76	1.79 – 1.76	1.79 – 1.76	1.79 – 1.76
R_{split}[1]	24.5 (76.4)	24.2 (75.4)	24.1 (74.9)	23.6 (78.3)	23.5 (79.1)
CC ½ (%)[1]	91.3 (37.2)	90.9 (31.1)	91.5 (38.7)	92.0 (34.9)	91.4 (32.8)
$I/\sigma I$[1]	3.24 (0.37)	3.26 (0.39)	3.31 (0.37)	3.24 (0.36)	3.18 (0.35)
Completeness (%)[1]	100.0 (100.0)	100.0 (100.0)	100.0 (100.0)	100.0 (100.0)	100.0 (100.0)
Multiplicity[1]	26.6 (19.4)	26.9 (19.6)	26.5 (19.4)	26.8 (19.7)	26.8 (19.6)
Unique Reflections[1]	29263 (1475)	29265 (1471)	29266 (1476)	29270 (1476)	29273 (1479)
Wilson B-factor ($Å^2$)	26.00	26.21	26.67	27.12	27.52

144 [1]High resolution statistics in parentheses

145 **Table S4**. Full data collection and refinement statistics for two SSX dose series reported in space group $P2_1$ (next pages). Data collection was
146 carried out at RT (21 °C) at an energy of X-ray Energy of 12.8 keV for 10 consecutive exposures to give dose points at 22 kGy interval.

147

Data collection statistics for the 22 kGy SSX dose-series

Data Collection	**22 kGy**	**44 kGy**	**66 kGy**	**88 kGy**	**110 kGy**
Number of Integrated Lattices	9015	9760	10114	9914	9533
Number of Merged Lattices	8989	9723	10079	9878	9506
Unit Cell a, b, c (Å)	39.5, 78.2, 48.1	39.4, 78.2, 48.1	39.4, 78.3, 48.0	39.4, 78.3, 48.0	39.4, 78.3, 48.0
β (°)	97.8	97.8	97.7	97.7	97.7
Resolution, overall (Å)	40.71 – 2.10	40.71 – 2.10	40.71 – 2.10	40.71 – 2.10	40.72 – 2.10
Resolution, high (Å)	2.14 – 2.10	2.14 – 2.10	2.14 – 2.10	2.14 – 2.10	2.14 – 2.10
R_{split}[1]	20.5 (24.7)	18.5 (20.2)	16.9 (19.9)	16.3 (20.9)	16.6 (24.9)
CC ½ (%)[1]	91.9 (83.8)	93.1 (89.2)	94.4 (89.5)	94.8 (90.4)	94.8 (87.2)
$I/\sigma I$[1]	9.47 (3.04)	9.70 (2.88)	9.14 (2.35)	8.28 (1.87)	7.34 (1.46)
Completeness (%)[1]	100.0 (100.0)	100.0 (100.0)	100.0 (100.0)	100.0 (100.0)	100.0 (100.0)
Multiplicity[1]	43.2 (29.7)	51.2 (35.5)	57.8 (39.9)	58.8 (39.0)	56.5 (35.0)
Unique Reflections[1]	16961 (855)	16959 (863)	16966 (866)	16966 (865)	16971 (861)
Wilson B-factor ($Å^2$)	18.52	20.31	22.63	24.80	26.59

Data Collection	**132 kGy**	**154 kGy**	**186 kGy**	**208 kGy**	**220 kGy**
Number of Integrated Lattices	8546	7476	6825	6297	5738
Number of Merged Lattices	8512	7442	6796	6255	5699
Unit Cell a, b, c (Å)	39.4, 78.4, 48.1	39.4, 78.4, 48.1	39.4, 78.4, 48.1	39.4, 78.3, 48.1	39.4, 78.3, 48.1
β (°)	97.7	97.7	97.7	97.7	97.7
Resolution, overall (Å)	40.70 – 2.10	40.71 – 2.10	40.72 – 2.10	40.72 – 2.10	40.73 – 2.10
Resolution, high (Å)	2.14 – 2.10	2.14 – 2.10	2.14 – 2.10	2.14 – 2.10	2.14 – 2.10
R_{split}[1]	16.8 (28.7)	17.7 (39.5)	18.4 (51.2)	18.5 (61.8)	19.6 (76.9)
CC ½ (%)[1]	95.3 (84.3)	94.9 (75.0)	94.5 (63.6)	95.6 (58.4)	95.6 (47.1)
$I/\sigma I$[1]	6.28 (1.15)	5.19 (0.92)	4.23 (0.77)	3.43 (0.70)	2.88 (0.63)
Completeness (%)[1]	100.0 (100.0)	100.0 (100.0)	100.0 (100.0)	100.0 (100.0)	100.0 (100.0)
Multiplicity[1]	50.6 (28.0)	44.9 (20.8)	41.4 (15.5)	38.1 (10.9)	34.3 (8.2)
Unique Reflections[1]	16977 (862)	16981 (860)	16983 (856)	16986 (859)	16989 (861)
Wilson B-factor ($Å^2$)	27.84	29.60	30.88	31.55	37.88

148 [1]High resolution statistics in parentheses

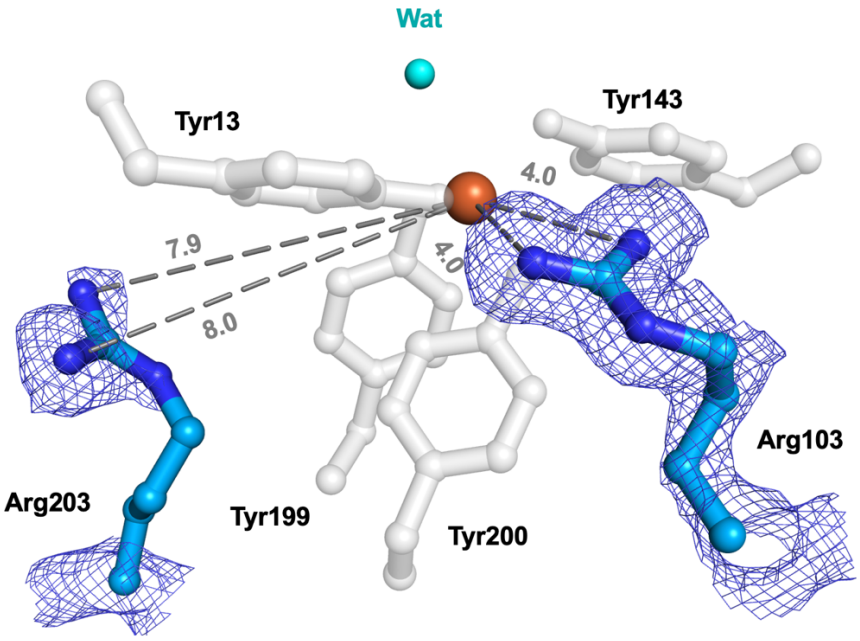

Figure S1. FutA (ferric state) characterized, neutron diffraction structure, compare **Fig. 2C**. The electron density ($2F_{obs} - F_{calc}$, blue, contoured at 1.5σ) reveals positioning of the side chain of Arg103 close to the tyrosinates, while the Arg203 side chain does not engage in interactions (similar to SFX structure **Fig. 2D**). Carbons shown blue, heteroatoms colored as in **Fig. 1**.

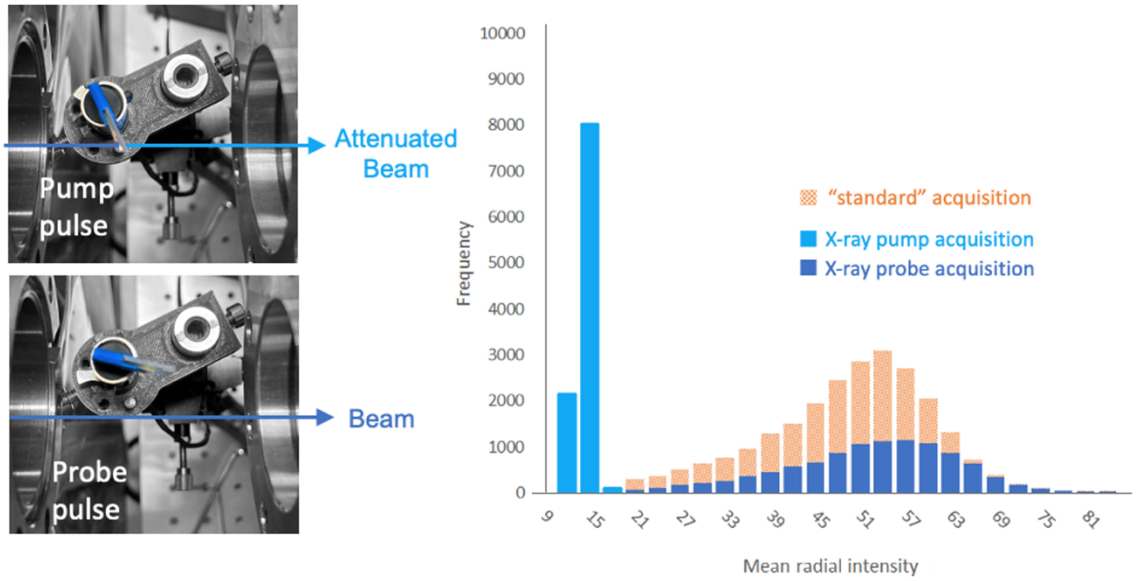

Figure S2: XFEL X-ray pump probe experiment. Left: a sapphire flipper-attenuator was placed in the path of the XFEL beam that was TTL triggered from a signal generator to move the wafer with alternating pulses, while two diffraction images were collected, corresponding to X-ray *pump* and X-ray *probe*. Right: resulting diffraction images are distinguished by mean intensity, where the X-ray *pump* shows lower radial intensities (light blue) compared with the X-ray *probe* (dark blue). For comparison, a data collecting resulting from a standard SFX experiment is shown (salmon).

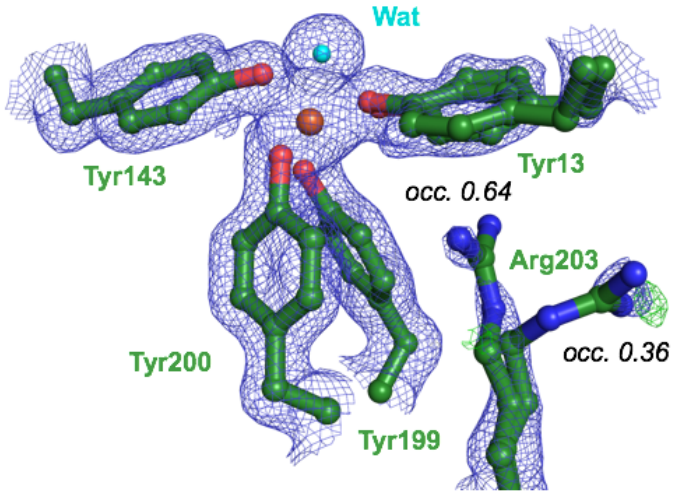

Figure S3. Refined SFX X-ray probe structure, compare **Fig. 4**. The side chain of Arg203 was refined in dual occupancy, as indicated. Density shown in blue is 2Fo-Fc at 1.5 σ, difference density Fo-Fc, shown in green, 3 σ; no negative difference density was observed. Heteroatoms colored as in **Fig. 1**.

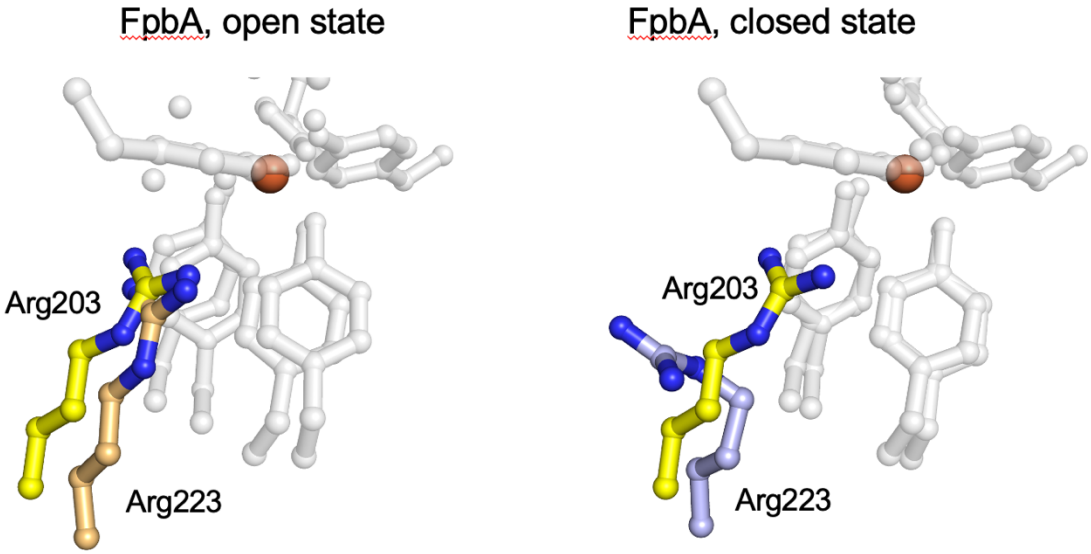

Figure S4: Overlay of ferrous bound *Prochlorococcus* MED4 FutA (yellow) with *Thermus thermophilus* FbpA in the open (light orange, PDB:3WAE) and closed confirmations (light purple, PDB:4ELR). As FpbA switches from an open to a closed conformation, a carbonate ion is lost and Arg233 is repositioned to maintain a net neutral charge in the binding site. The repositioning of Arg233 in FbpA is highly similar to the structural switch of Arg203 in FutA. Comparison of RT rotation data with the SSX structure, dose point at 88 kGy.

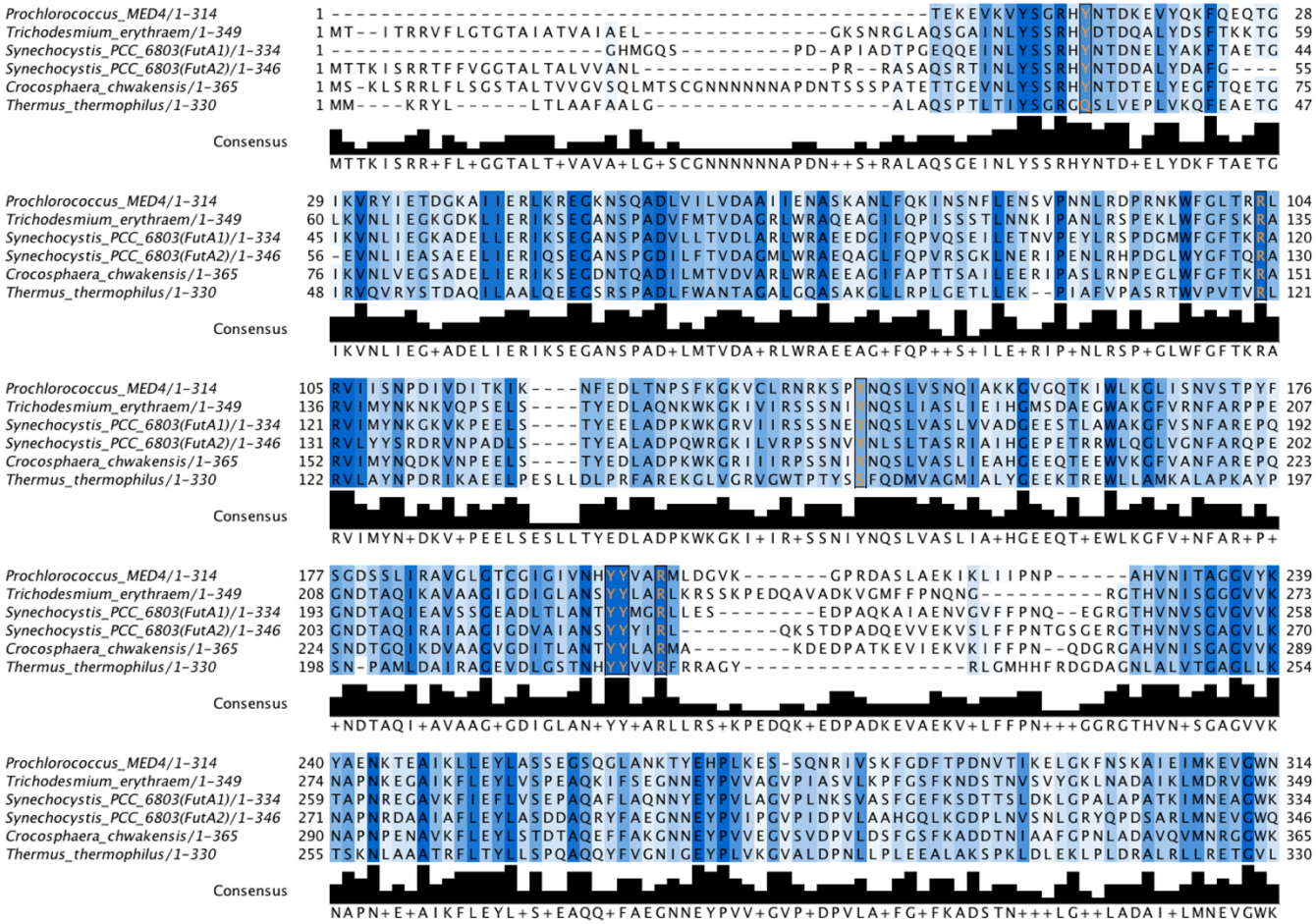

Figure S5: Multiple sequence alignment of the FutA homologues from *Prochlorococcus* MED4, *Trichodesmium erythraeum*, *Synechocystis* PCC 6803, *Crocosphaera chwakensis*, and *Thermus thermophilus* carried out with Clustal Omega (21) and Jalview (22). Iron coordinating amino acids in Prochlorococcus MED4 are shown in orange text. The consensus graph indicates the modal residue and the number of times the modal residue appears at each position. "+" denotes positions where the modal residue is shared by more than one amino acid type. The blue shading indicates the degree of conservation of the physio-chemical properties of the amino acids at each position.

References

1. J. J. Almagro Armenteros *et al.*, SignalP 5.0 improves signal peptide predictions using deep neural networks. *Nature Biotechnology* **37**, 420-423 (2019).
2. J. H. Beale *et al.*, Successful sample preparation for serial crystallography experiments. *Journal of Applied Crystallography* **52**, 1385-1396 (2019).
3. S. Horrell *et al.*, Fixed Target Serial Data Collection at Diamond Light Source. *J Vis Exp* 10.3791/62200 (2021).
4. W. Kabsch, XDS. *Acta Crystallographica Section D* **66**, 125-132 (2010).
5. P. R. Evans, G. N. Murshudov, How good are my data and what is the resolution? *Acta Crystallographica Section D* **69**, 1204-1214 (2013).
6. Z. Otwinowski, W. Minor, Processing of X-ray diffraction data collected in oscillation mode. *Methods in Enzymology* **276**, 307-326 (1997).
7. G. Winter *et al.*, DIALS: implementation and evaluation of a new integration package. *Acta Crystallographica Section D* **74**, 85-97 (2018).
8. M. Uervirojnangkoorn *et al.*, Enabling X-ray free electron laser crystallography for challenging biological systems from a limited number of crystals. *Elife* **4** (2015).
9. P. Howell, G. Smith, Identification of heavy-atom derivatives by normal probability methods. *Journal of applied crystallography* **25**, 81-86 (1992).
10. T. Nakane *et al.*, Data processing pipeline for serial femtosecond crystallography at SACLA. *Journal of Applied Crystallography* **49**, 1035-1041 (2016).
11. J. Hattne *et al.*, Accurate macromolecular structures using minimal measurements from X-ray free-electron lasers. *Nature Methods* **11**, 545-548 (2014).
12. A. Vagin, A. Teplyakov, MOLREP: an Automated Program for Molecular Replacement. *Journal of Applied Crystallography* **30**, 1022-1025 (1997).
13. P. Emsley, B. Lohkamp, W. G. Scott, K. Cowtan, Features and development of Coot. *Acta Crystallogr D Biol Crystallogr* **66**, 486-501 (2010).
14. G. N. Murshudov *et al.*, REFMAC5 for the refinement of macromolecular crystal structures. *Acta Crystallographica Section D* **67**, 355-367 (2011).
15. C. R. Harris *et al.*, Array programming with NumPy. *Nature* **585**, 357-362 (2020).
16. W. McKinney, Data Structures for Statistical Computing in Python. *Proceedings of the 9th Python in Science Conference* **445**, 56-61 (2010).
17. P. Virtanen *et al.*, SciPy 1.0: fundamental algorithms for scientific computing in Python. *Nature Methods* **17**, 261-272 (2020).
18. S. Seabold, J. Perktold, Statsmodels: Econometric and Statistical Modeling with Python. *Proceedings of the 9th Python in Science Conference* **445**, 92-96 (2010).
19. J. D. Hunter, Matplotlib: A 2D Graphics Environment. *Computing in Science & Engineering* **9**, 90-95 (2007).
20. S. Grazulis *et al.*, Crystallography Open Database (COD): an open-access collection of crystal structures and platform for world-wide collaboration. *Nucleic Acids Res.* **40**, D420-427 (2012).
21. F. Sievers *et al.*, Fast, scalable generation of high-quality protein multiple sequence alignments using Clustal Omega. *Molecular Systems Biology* **7**, 539 (2011).
22. A. M. Waterhouse, J. B. Procter, D. M. A. Martin, M. Clamp, G. J. Barton, Jalview Version 2—a multiple sequence alignment editor and analysis workbench. *Bioinformatics* **25**, 1189-1191 (2009).
23. D. Polyviou *et al.*, Structural and functional characterization of IdiA/FutA (Tery_3377), an iron-binding protein from the ocean diazotroph Trichodesmium erythraeum. *Journal of Biological Chemistry* **293**, 18099-18109 (2018).
24. P. Lu *et al.*, Functional characterisation of two ferric-ion coordination modes of TtFbpA, the periplasmic subunit of an ABC-type iron transporter from Thermus thermophilus HB8. *Metallomics* **11**, 2078-2088 (2019).
25. S. Wang *et al.*, A novel mode of ferric ion coordination by the periplasmic ferric ion-binding subunit FbpA of an ABC-type iron transporter from Thermus thermophilus HB8. *Acta Crystallographica Section D* **70**, 196-202 (2014).